Journal of Controlled Release 368 (2024) 566–579

Contents lists available at ScienceDirect

Journal of Controlled Release

journal homepage: www.elsevier.com/locate/jconrel

Iron-carbohydrate complexes treating iron anaemia: Understanding the nano-structure and interactions with proteins through orthogonal characterisation

Leonard Krupnik [a,b,c], Jonathan Avaro [a], Marianne Liebi [d,e], Neda Iranpour Anaraki [a,b,c], Joachim Kohlbrecher [f], Alla Sologubenko [g], Stephan Handschin [g], Andrzej J. Rzepiela [g], Christian Appel [d], Tiberiu Totu [b,h,i], Clement E. Blanchet [j], Amy E. Barton Alston [k], Reinaldo Digigow [k], Erik Philipp [k], Beat Flühmann [k], Bruno F.B. Silva [a], Antonia Neels [a,c,*], Peter Wick [b,**]

[a] Center for X-ray Analytics, Empa, Swiss Federal Laboratories for Materials Science and Technology, Lerchenfeldstrasse 5, St. Gallen 9014, Switzerland
[b] Particles-Biology Interactions Laboratory, Empa, Swiss Federal Laboratories for Materials Science and Technology, Lerchenfeldstrasse 5, 9014 St. Gallen, Switzerland
[c] Department of Chemistry, University of Fribourg, Chemin du Musée 9, 1700 Fribourg, Switzerland
[d] Photon Science Division, PSI Paul Scherrer Institute, Villigen CH-5232, Switzerland
[e] Institute of Materials, Ecole Polytechnique Fédérale de Lausanne (EPFL), CH-1015 Lausanne, Switzerland
[f] Laboratory for Neutron Scattering, PSI Paul Scherrer Institute, Villigen CH-5232, Switzerland
[g] Scientific Center for Optical and Electron Microscopy, ScopeM, ETH Zürich, 8093 Zürich, Switzerland
[h] ETH Zurich, Department of Health Sciences and Technology (D-HEST), CH-8093 Zurich, Switzerland
[i] SIB, Swiss Institute of Bioinformatics, CH-1015 Lausanne, Switzerland
[j] European Molecular Biology Laboratory, Hamburg Outstation, Notkestrasse 85, Hamburg 22603, Germany
[k] CSL Vifor, Flughofstrasse 61, CH-8152 Glattbrugg, Switzerland

ARTICLE INFO

Keywords:
Iron deficiency anaemia
Nanoparticles (NPs)
Non-biological complex drugs (NBCDs)
Iron-carbohydrate complexes
Small-angle x-ray scattering (SAXS)
Small-angle neutron scattering (SANS)

ABSTRACT

Intravenous (IV) iron-carbohydrate complexes are widely used nanoparticles (NPs) to treat iron deficiency anaemia, often associated with medical conditions such as chronic kidney disease, heart failure and various inflammatory conditions. Even though a plethora of physicochemical characterisation data and clinical studies are available for these products, evidence-based correlation between physicochemical properties of iron-carbohydrate complexes and clinical outcome has not fully been elucidated yet. Studies on other metal oxide NPs suggest that early interactions between NPs and blood upon IV injection are key to understanding how differences in physicochemical characteristics of iron-carbohydrate complexes cause variance in clinical outcomes. We therefore investigated the core-ligand structure of two clinically relevant iron-carbohydrate complexes, iron sucrose (IS) and ferric carboxymaltose (FCM), and their interactions with two structurally different human plasma proteins, human serum albumin (HSA) and fibrinogen, using a combination of cryo-scanning transmission electron microscopy (cryo-STEM), x-ray diffraction (XRD), small-angle x-ray scattering (SAXS)

Abbreviations: NPs, Nanoparticles; IS, Iron sucrose; FCM, Ferric carboxymaltose; HSA, Human serum albumin; SAXS, Small-angle x-ray scattering; SANS, Small-angle neutron scattering; NBCDs, Non-biological complex drugs; CQA, Critical quality attributes; IV, Intravenous; PDI, Polydispersity index; MPS, Mononuclear phagocyte system; XRD, X-ray diffraction; cryo-(S)TEM, Cryo-(scanning) transmission electron microscopy; GIFT, Generalised indirect Fourier transform; SEC, Size-exclusion chromatography; AFM, Atomic-force microscopy; DLS, Dynamic light scattering; (HAA)DF, (High-angle annular) dark field; (LAA)DF, (Low-angle annular) dark field; BF, Bright field; SLD, Scattering length density; EDS, Energy dispersive x-ray spectroscopy.

* Corresponding author at : Center for X-ray Analytics, Empa, Swiss Federal Laboratories for Materials Science and Technology, Lerchenfeldstrasse 5, St. Gallen 9014, Switzerland.

** Corresponding author at: Laboratory for Particles-Biology Interactions, Empa, Swiss Federal Laboratories for Materials Science and Technology, Lerchenfeldstrasse 5, St. Gallen 014, Switzerland.

E-mail addresses: antonia.neels@empa.ch (A. Neels), peter.wick@empa.ch (P. Wick).

https://doi.org/10.1016/j.jconrel.2024.02.044
Received 27 December 2023; Received in revised form 24 February 2024; Accepted 27 February 2024
Available online 14 March 2024

and small-angle neutron scattering (SANS). Using this orthogonal approach, we defined the nano-structure, individual building blocks and surface morphology for IS and FCM. Importantly, we revealed significant differences in the surface morphology of the iron-carbohydrate complexes. FCM shows a localised carbohydrate shell around its core, in contrast to IS, which is characterised by a diffuse and dynamic layer of carbohydrate ligand surrounding its core. We hypothesised that such differences in carbohydrate morphology determine the interaction between iron-carbohydrate complexes and proteins and therefore investigated the NPs in the presence of HSA and fibrinogen. Intriguingly, IS showed significant interaction with HSA and fibrinogen, forming NP-protein clusters, while FCM only showed significant interaction with fibrinogen. We postulate that these differences could influence bio-response of the two formulations and their clinical outcome. In conclusion, our study provides orthogonal characterisation of two clinically relevant iron-carbohydrate complexes and first hints at their interaction behaviour with proteins in the human bloodstream, setting a prerequisite towards complete understanding of the correlation between physicochemical properties and clinical outcome.

1. Introduction

Iron deficiency anaemia is a global health problem with an estimated one billion people affected [1–4]. To treat iron deficiency anaemia, oral and intravenous (IV) iron-carbohydrate complexes have been developed, aiming to replenish the body's physiological iron storage and transport systems [5,6]. In the last decades, IV iron-carbohydrate complexes have gained increased popularity owing to their improved bioavailability, reduced gastrointestinal side effects and shortened iron store repletion time compared to their oral counterparts [7–9]. IV iron-carbohydrate complexes are comprised of an iron-oxyhydroxide core bound to a carbohydrate ligand [8,10–12]. These complexes are nanoparticles (NPs) that are classified as non-biological complex drugs (NBCDs) with several brands of slightly different core-ligand properties available on the market [8,13,14]. Iron-carbohydrate complexes were specifically engineered to facilitate uptake by macrophages, which then transport the complexes to the key organs of the mononuclear phagocyte system (MPS), the liver and spleen to finally be biodegraded to mobilise usable iron [15,16]. In contrast to un-complexed iron oxyhydroxide, iron-carbohydrate complexes avoid adverse effects due to excessive iron release [16,17]. This design was inspired by endogenous serum ferritin, which stores ferric iron by creating an iron-protein complex, releasing iron under homeostatic demand [18–20]. The chemistry of the bonded carbohydrate is an important driver of the pharmacokinetic and pharmacodynamic differences in these products, as it governs the NP's surface characteristics (e.g. surface charge and interaction with plasma proteins) and therefore the biological uptake of the iron-carbohydrate complex [16,21]. In this regard, iron-carbohydrate complexes with variations in the ligand were shown to be associated with changes in clearance kinetics from the serum, tissue distribution or release rates of bioactive iron from the NPs [15,18,20,22,23]. However, even though a wealth of physicochemical data and clinical studies are available, evidence-based correlation between physicochemical properties of the iron-carbohydrate complexes and clinical outcome has not been entirely described.

When iron-carbohydrate complexes are administered intravenously, they are taken up by macrophages via pathways that have not been completely elucidated and are then delivered to the MPS [6,15,16,20]. Once within the MPS, the carbohydrate ligand is thought to be biodegraded in the endosomal and lysosomal structures [20,24]. The iron is then released into a low-molecular-weight iron pool and stored safely within ferritin, an intracellular iron-storing protein complex [25]. From there, it is transported via ferroportin to transferrin, which facilitates the redistribution of iron to the bone marrow upon normal iron physiologic signaling [16,26]. While the exact details of this proposed uptake mechanism(s) have not been fully understood, studies on metal oxide NPs suggest the early interactions between NPs and blood to be fundamental to understanding how differences in physicochemical parameters result in different clinical responses [27]. When NPs enter biological systems, processes such as NP agglomeration and chemical alterations may be induced by the biological media, thus reducing colloidal stability. Referred to as biotransformation, these phenomena have been shown to alter the NP's pharmacological properties such as biodistribution, toxicity and cellular response [15,28]. Changes to the 3-dimensional structural identity and thus, the pharmacological profile of a NP, can also occur when serum proteins interact with the NP surface. These protein-NP interactions within biological fluids promote adsorption of the protein into the NP interface, which then causes formation of a protein corona [29,30]. As demonstrated by many studies, formation of a protein corona may change hydrodynamic diameter [31,32] and alter colloidal stability [33–35] of the NP and can even influence the NP's cellular uptake [36–38] and/or bio-distribution [21].

The findings from studies of metal oxide NPs indicate that early biotransformation events and NP-protein interactions are crucial to understanding structure-function relationships [27,39]. While there is knowledge on this for other metal oxide NPs, there is still a need to understand how physicochemical changes of iron-carbohydrate complexes affect the biological interface and hence the bio-response, and how these surface structure changes may be applied to identify their critical quality attributes (CQA). The US Food and Drug Administration (FDA) [40] and the European Medicines Agency (EMA) [41] have recognized the need to fully understand CQAs to comprehend the relationship between physicochemical properties and in vivo disposition of iron-carbohydrate complexes [42].

Therefore, our study aims to use orthogonal methodologies to comprehensively analyse the nano-structure, individual building blocks and physicochemical properties of the iron-carbohydrate complexes and their evolution during their interaction with physiological media (0.9% *w/v* NaCl solution) and two structurally different and highly abundant plasma proteins, human serum albumin (HSA) and fibrinogen. To achieve these aims, two clinically relevant iron-carbohydrate complexes (Scheme 1), iron sucrose (IS) and ferric carboxymaltose (FCM), were characterised by microscopy and scattering techniques, namely cryo-scanning transmission electron microscopy (cryo-STEM), x-ray diffraction (XRD), small-angle x-ray scattering (SAXS) and small-angle neutron scattering (SANS). With this approach, iron-carbohydrate complexes and their interactions with serum proteins can be more precisely and conclusively described compared to previous studies, setting a path to correlate physicochemical properties with bio-responses in vivo and clinical outcome.

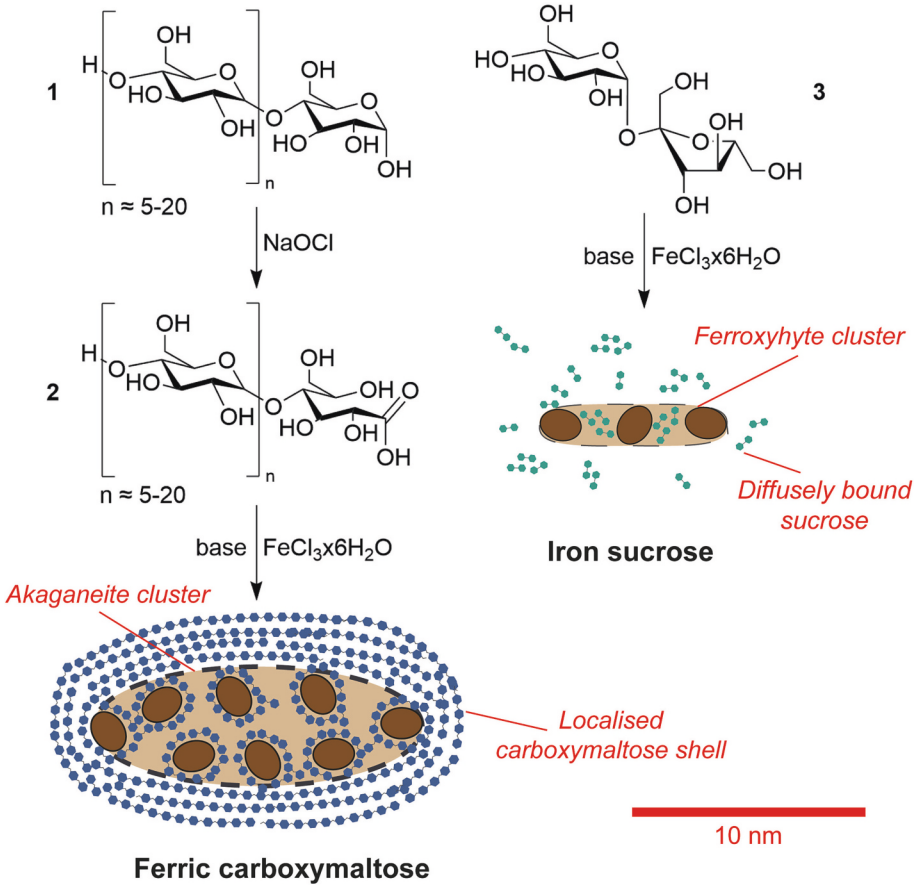

Scheme 1. Structure, composition and synthesis route of ferric carboxymaltose (FCM) and iron sucrose (IS) (scale bar: 10 nm). Sizes of sugar molecules do not correspond to the scale bar.

2. Materials and methods

2.1. Iron-carbohydrate complexes

Iron sucrose (Venofer®, 20 mg Fe/mL in 5 mL ampoules, Mat No.: 6057821, Kd. Ch..: 916211, Ch. B: 00564818, expiry date: 2022.11, CSL Vifor, St. Gallen, Switzerland) and ferric carboxymaltose (Ferinject®, 50 mg Fe/mL in 10 mL ampoules, VIT-45 YV080, Lot No.: 7590012A, expiry date: 2020.05, CSL Vifor, St. Gallen, Switzerland) were obtained directly from the manufacturer. All materials were kept sealed and stored at room temperature until the study.

2.2. Carbohydrates

Sucrose and oxidised carboxymaltose were obtained directly from the manufacturer (CSL Vifor, St. Gallen, Switzerland).

2.3. NaCl solution

Sterile saline buffer 0.9% *w/v* was purchased from Bichsel AG and was used for the dilution of the iron-carbohydrate complexes.

2.4. Human serum albumin (HSA)

HSA is one of the most abundant protein in the human blood with concentrations ranging between 35 and 50 mg/mL. It has a molecular weight of 66.4 kDa, is very robust regarding pH, temperature changes and de-folding when interacting with a variety of ligands and does not exhibit any agglomeration in organic as well as aqueous solutions [43–45]. Since experiments are conducted in a pH range of 4 to 7.4, HSA should exist in its N-form, which is characterised by a heart-shaped structure [45]. The product (200 mg/mL) was purchased from CSL Behring (Pennsylvania, USA) and stored at room temperature under light protection.

2.5. Fibrinogen

Fibrinogen is a highly abundant plasma protein responsible for blood clotting through conversion into fibrin by the presence of thrombin. It is an elongated molecule with a molecular weight of 340 kDa that consists of three domain pairs that are each bonded through disulfide chains [46,47]. Fibrinogen is stable at high concentrations in 0.9% NaCl buffer, but should not be vortexed as this can lead to visible agglomeration. Fibrinogen (50–70% protein) was purchased from Merck Sigma Aldrich and stored at −20°C.

2.6. Small-angle x-ray scattering (SAXS)

SAXS studies of the stock solutions and dilutions of the iron-carbohydrate complexes were performed at the cSAXS beamline, Swiss Light Source (SLS) at the Paul Scherrer Institute (PSI, Switzerland). SAXS studies of the carbohydrate ligands of iron sucrose (IS) and ferric carboxymaltose (FCM) were performed at the P12 beamline of EMBL at the PETRA III storage ring (DESY, Hamburg). All other SAXS studies were carried out using a laboratory X-ray setup (Bruker Nanostar, Bruker AXS GmbH, Karlsruhe, Germany). More detailed information on the SAXS set-up is available in the SI.

2.7. X-ray diffraction (XRD)

XRD measurements were performed using a Stoe IPDS-II instrument equipped with graphite-monochromatised Mo-K_α radiation (λ = 0.71073 Å, 40 mA, 50 kV, beam diameter of 0.5 mm) and an image plate detector. A molybdenum X-ray source was used to ensure a significant enhancement of the signal-to-noise ratio strongly impaired by the high fluorescence of iron-containing compounds when using the copper X-ray sources. The iron-carbohydrate complex stock solutions were filled into quartz capillaries (1 mm, Hilgenberg GmbH), placed in a rotating sample holder and measured in transmission mode for 1 h. The azimuthal data integration of the 2D diffraction pattern resulted in a 1D diffraction profile.

2.8. Small-angle neutron scattering (SANS)

SANS measurements were performed at the SANS-I beamline at the Swiss Spallation Neutron Source (SINQ) at Paul Scherrer Institute, Switzerland, using neutron wavelengths of $\lambda = 0.6$ nm (for FCM) and 0.5 nm (for IS) and a wavelength resolution ($\Delta\lambda/\lambda$) of approximately 10% (FWHM). A resolvable q-range of $0.07 \leq q \leq 5\ nm^{-1}$ was achieved using two sample-detector distances of 2 m and 8 m. The samples were measured in Hellma quartz cuvettes (Hellma 100-QS, HL100–1-40, Hellma Analytics) with a path length of 1 mm. The cuvettes were positioned in front of the beam on a thermostatic sample holder set at 25°C. A two-dimensional 128 × 128 elements ^{3}He gas-detector with a pixel size of 7.5 × 7.5 mm^2 was used to detect the scattered neutrons. The measured data was isotropic azimuthally averaged for each q-value, corrected for transmission and non-uniform detector efficiency using the scattering of a water sample and subtracted by the scattering contribution of the quartz cuvette using the BERSANS software [48]. To obtain the final data, the incoherent scattering was subtracted and the data points were thinned out by averaging neighbouring data points depending on the error bar and q difference using Matlab 2022.

2.9. Cryo-(scanning) transmission electron microscopy (cryo-(S)TEM) and image analyses

Complex TEM studies of the iron-carbohydrate complexes were performed at ~80 K employing both operation modes of TEM, parallel illumination (TEM mode) and conical illumination (scanning TEM, i.e. STEM mode). The vitrified specimen material and stable low-temperature environment around the specimen inside the TEM instrument helped to preserve the most natural state and structural and thermal stability of the specimen during the studies. Electron radiation damage and any kinetic effects leading to the coalescence and phase transformations of the iron-carbohydrate complexes were minimised or eliminated at liquid nitrogen temperature. Cryo-TEM analyses provided statistically representative and low electron dose information relying on the automated and semi-automated routines for data acquisition from large areas of the TEM specimens. Data acquisitions during cryo-STEM measurements were performed manually to ensure the most optimal focus of the nano-sized features and minimal or none electron beam-induced damage from the highly focused STEM probe. The cryo-STEM morphological analyses were complemented by analytical studies using the energy dispersive X-ray spectroscopy (EDS) employed in the spectrum image mode of EDS STEM. A detailed description of the conditions and parameters of cryo-TEM and cryo-STEM experimental procedures, EDS as well as the information on the manual and automated image analyses, are available in the SI.

3. Results and discussion

3.1. Structural characterisation of iron-carbohydrate complexes

3.1.1. Morphology of iron-carbohydrate complexes

Morphological and analytical studies of iron sucrose (IS) and ferric carboxymaltose (FCM) were performed by cryo-scanning transmission electron microscopy (cryo-STEM) and statistically verified by cryo-TEM. Then, x-ray diffraction (XRD) studies of nanoparticle (NP) stock solutions were carried out to identify the crystal structure and ascertain the size of the iron core of the iron-carbohydrate complexes. Using these STEM and XRD data as inputs, the structure of both IS and FCM was modelled in solution using small-angle x-ray scattering (SAXS) and small-angle neutron scattering (SANS), particularly aiming at the morphology of the iron core, possibly formed clusters (i.e. size, shape, polydispersity and arrangement) and the morphology of the stabilising carbohydrate ligand.

Fig. S1a–c shows the representative cryo-STEM data of FCM, including three different signals: bright field (BF STEM), high-angle annular dark field (HAADF STEM) and low-angle annular dark field (LAADF STEM). LAADF STEM provided the prominent diffraction signal of the iron cores of the NPs due to their crystalline nature, while the carbohydrate ligand signal was very weak. LAADF signal micrographs were chosen as the most suitable for both automated and manual image analysis routines. The energy dispersive X-ray spectroscopy (EDS) STEM verified the Fe signal within the clusters of IS and FCM (see SI and Fig. S2).

3.1.1.1. Iron sucrose. The LAADF electron micrographs of an 1:10 dilution of IS are shown in Fig. 1a. For IS, clusters with a high aspect ratio were visible. These clusters varied in elongation, occasionally connecting to form larger agglomerates (Fig. 1a, red arrows). The clusters consisted of multiple crystalline iron cores, often arranged equidistantly within the cluster. These iron cores will from now on be referred to as single NPs. Single NPs only attached at the tips of the clusters rather than on the lateral edges, indicating that clusters only grow into one spatial dimension. Additionally, a significant number of free single NPs were visible.

More accurate assessment of the cluster morphology as well as the inter-particle distance within a cluster was performed using manual image analysis (see SI, Fig. S1). Manual image analysis gave a single NP size of 2.0 nm and an average inter-particle distance along a cluster to be within the 2.0 to 3.0 nm interval. The length and width of the clusters were estimated at 9.2 nm and 3.6 nm on average (Table S1).

To obtain reliable statistical data on the cluster morphology (cluster diameter, cluster fraction and cluster shape) automated image analysis using a machine-learning algorithm (see SI, Fig. S3) was performed. The distribution of equivalent diameters for IS was very broad and statistical analysis could not verify the existence of more than one size population (Fig. 1b). The mean equivalent diameter of the clusters was 6.7 ± 2.4 nm (Table 1, see SI for more details). Interestingly, several maxima (4.0, 6.0, 8.5, 10.5 and 12.5 nm) with an average distance of 2.0–2.5 nm between each other were observed in the histogram. These quantised maxima suggest defined clusters (e.g. dimers, trimers or multimers) built up by linear alignment of single NPs at a certain inter-particle distance, pointing towards our work hypothesis that the growth of the clusters happens only in one spatial dimension (unidirectionally). Based on this cluster formation process, the size of the single NPs, size of the clusters and inter-particle distance (2.0 nm, 6.7 nm and 2.0–3.0 nm, respectively) an average of two to three NPs per cluster was assumed. For further analysis of the cluster shape using the degree of eccentricity (as the deviation from the spherical shape), and the cluster fraction see the SI and Fig. S4a and c.

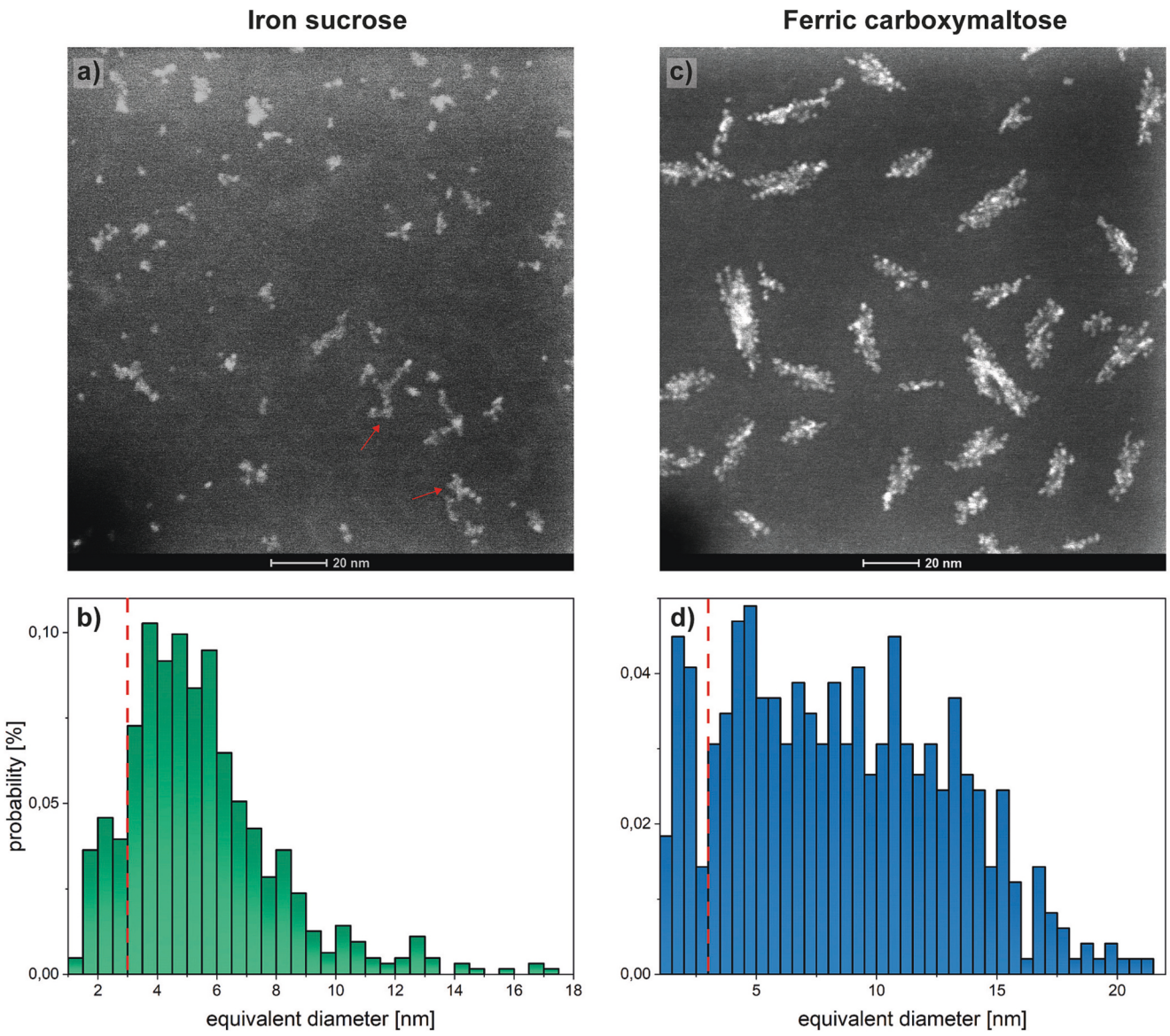

Fig. 1. Low-angle annular dark-field (LAADF) cryo-scanning transmission electron microscopy (STEM) micrographs (scale bar: 20 nm) of iron sucrose (IS) and ferric carboxymaltose (FCM) at 1:10 dilution in milliQ-water together with the results from automated image analysis. (a) IS forms needle-like clusters made up of single nanoparticles (NPs). Agglomerates formed by attachment of IS clusters are indicated with red arrows. (c) FCM forms two populations of clusters: larger clusters made up of multiple single NPs and smaller clusters made up of two single NPs. Histogram of equivalent diameters (bin = 0.5) determined by automated image analysis for an 1:10 dilution of (b) IS and (d) FCM. Equivalent diameters left to the red dotted line are associated with single NPs. (For interpretation of the references to colour in this figure legend, the reader is referred to the web version of this article.)

Table 1
Structural parameters determined from manual and automated image analysis of cryo-scanning transmission electron microscopy (cryo-STEM) data of iron sucrose (IS) and ferric carboxymaltose (FCM) for single nanoparticles (NPs) and clusters. The mode of each size population of FCM, determined by statistical analysis (Fig. S5), is also shown.

	Contribution	Mean eq. diameter [nm]	Eccentricity	Cluster fraction	Mode [nm]
Iron sucrose	**Single NPs**	2.0 ± 1.0	0.64 ± 0.19	0.127	/
	Clusters	6.7 ± 2.4	0.69 ± 0.20	0.875	/
Ferric carboxymaltose	**Single NPs**	2.0 ± 1.0	0.72 ± 0.19	0.118	1.7
	Clusters	9.3 ± 4.1	0.84 ± 0.16	0.882	Small: 4.4 Large: 10.5

3.1.1.2. Ferric carboxymaltose. For FCM, well-separated clusters with a larger minor diameter than those of IS were identified (Fig. 1c). The clusters were comprised of multiple crystalline single NPs arranged as strands equidistantly within the cluster, similar to IS. However, they seemed to attach at both the tips and the lateral edges of the clusters, indicating that single NPs grow into two spatial dimensions (bidirectionally). Additionally, a significantly smaller number of free single NPs was observed compared to IS.

From manual image analysis of the LAADF micrograph of FCM (Fig. S1d–f), it was clear that single NPs had a size between 1.9 and 2.2 nm

and an average inter-particle distance of 2.5 to 3.0 nm. The width of the clusters was 5.7 nm and the length was 17.0 nm (Table S1).

Automated image analysis showed the distribution of equivalent diameters to be very broad (Fig. 1d). The mean equivalent diameter of the clusters was 9.3 ± 4.1 nm, which is significantly higher compared to IS (Table 1). A more in-depth statistical analysis of the histogram (see SI) indicated three distinct peaks in the histogram, implying the existence of three size populations (Fig. S5a). First, a peak with a mode of 1.7 nm, which was associated with single NPs in accordance with the value calculated from the manual image analysis, was observed. Secondly, a peak at 4.4 nm was observed, corresponding to a distinct population of particularly stable small clusters formed by a NP dimer (based on a single NP size of 2 nm and an inter-particle distance of 2.5–3.0 nm) as seen in Fig. S6. Lastly, a peak with a mode of 10.5 nm was observed, associated with particularly stable large clusters. These findings indicate the arrangement of single NPs preferably into smaller (4.4 nm) clusters and larger clusters (10.5 nm), while less stable clusters also exist in between the distribution. In the case of FCM, the average number of single NPs per cluster is difficult to estimate as clusters exhibit bidirectional growth. For further analysis of the cluster shape and cluster fraction see the SI and Fig. S4b, c.

Our findings for both complexes agree well with previous (cryo)-TEM studies on IS and FCM. In these, IS had a size between 2 and 5 nm and was spherically shaped [11,49,50]. However, due to a significantly lower signal-to-noise ratio, IS clusters were most likely interpreted as single NPs leading to an overestimation of the single NP size in some of the studies. For FCM, Jahn et al. determined a size of 11.7 ± 4.4 nm corresponding to FCM clusters, while the single NP size was not definable [49]. The ability to measure single NPs of FCM for the first time demonstrates the improvement brought by our cryo-STEM approach.

3.1.2. *Crystal structure and crystallite size of the single NPs*

The size of IS and FCM single NPs and their crystal structure was determined by XRD using the NP stock solutions. The goal was to obtain further information on the NP size and the crystallographic phase of the single NP building blocks of IS and FCM and to confirm the results of the prior cryo-STEM experiments. A high number of broad and overlapping diffraction peaks were observed for FCM (Fig. 2b). The size of FCM single NPs was estimated by calculating the mean coherence length, resulting in a determined value of 2.6 ± 1.1 nm. This was consistent with results from the cryo-STEM analysis but differed from earlier XRD studies [49,51] done on powders rather than solutions of FCM. Those crystallite sizes were estimated between 4 and 5 nm, significantly higher than our solution measurements, which was explained by a high standard uncertainty often seen for small-sized NPs. Analysis of the crystal phase indicated an akaganeite structure (β-FeOOH, #12 I2/m, COD No. 9001319), which is in accordance with earlier studies [52]. A significantly lower number of broad diffraction peaks was observed for IS (Fig. 2a). The mean coherence length was estimated as 3.9 nm, which was slightly higher compared to our cryo-STEM experiments but is consistent with previous XRD studies [11,49,51] The analysis of present crystal phases gave the best correspondence to ferroxyhyte (δ-FeOOH, #164 P-3 m, COD No. 1008762) as the main phase with the presence of other possible minor phases such as goethite (α-FeOOH, space group #62 Pnma, COD No. 9002158) and lepidocrocite (γ-FeOOH, space group #63 Cmc21, COD No. 9015231). Our work accentuates the ambiguity raised by previous XRD studies, which have associated IS crystallinity with akaganeite, lepidocrocite or ferrihydrite crystal structure; those ambiguities are mostly due to the general low crystallinity of the sample and the limited number of diffraction peaks [11,52].

3.1.3. *Model of the nano-structure of the iron core of iron-carbohydrate complexes*

The knowledge gained from cryo-STEM and XRD on the nano-structure and individual building blocks of both iron-carbohydrate complexes was used to further describe and refine these structures using SAXS. Due to a significant difference in scattering length density (SLD) between iron oxyhydroxide and carbohydrate with respect to the SLD of the solvent, the scattering intensity in SAXS stems mostly from the iron core. However, an elevated background at the high q region was observed for both IS and FCM related to their unbound sugars (see SI and Fig. S7).

To study possible dilution effects, increasing dilutions of iron-carbohydrate complexes in milliQ-water were prepared.

3.1.3.1. Iron sucrose. The SAXS curves of IS (Fig. 3a) represented multi-component power law profiles typical for clustered and/or polydisperse systems at all dilution ratios, which is consistent with the broad size distributions observed in cryo-STEM. At low q, all scattering curves exhibited a plateau before the intensity started to decay until approximately $q = 2.0\ \mathrm{nm}^{-1}$. For the 1:10 dilution of IS, however, a slight upturn at very low q was evident, which further increased at 1:50 dilution ratios (Fig. 3a, black arrows). This was explained by the scattering of very large domains, whose size was estimated to be at least 100 nm, which will be discussed later on.

To fit the scattering curves of IS with an appropriate model, several assumptions based on the prior cryo-STEM and XRD data were used. The best obtained fit for IS was realised with two components: i) clusters

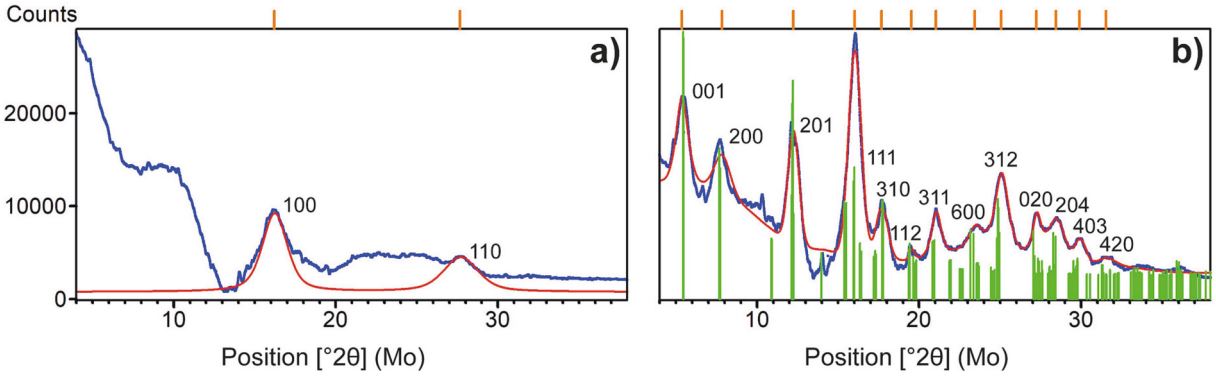

Fig. 2. X-ray diffraction (XRD) patterns for IS and FCM. (a) XRD pattern of IS (blue) showing the indexed main phase ferroxyhyte (red, COD: 1008762). (b) XRD pattern of FCM (blue) showing the indexed akaganeite phase (red, COD: 9001319). Green shows the respective phase patterns for FCM with the corresponding hkl-values. Red shows the Rietveld refined phase information. (For interpretation of the references to colour in this figure legend, the reader is referred to the web version of this article.)

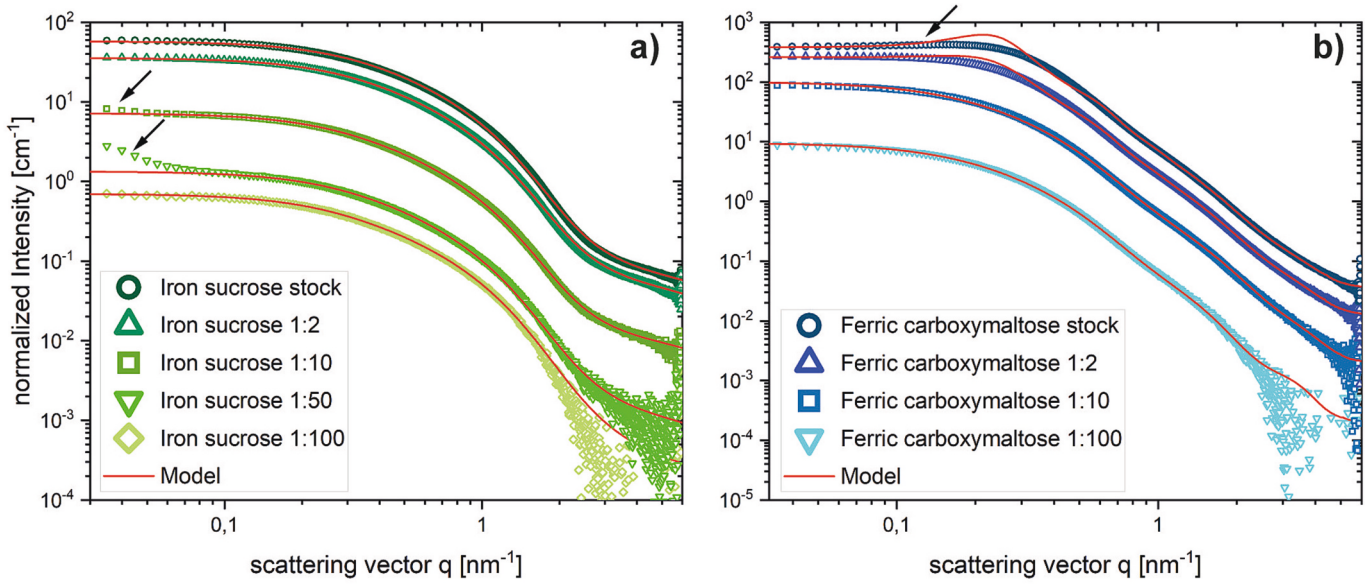

Fig. 3. Small-angle x-ray scattering (SAXS) data and model fits of (a) IS and (b) FCM at stock solutions and different dilutions (1:2, 1:10, 1:50 and 1:100). The SAXS model describes IS as prolate spheroidal clusters made up of single NPs with unbound sucrose in solution. The SAXS model describes FCM as large prolate spheroidal clusters made up of single NPs, small prolate spheroidal clusters made up of two single NPs and free single NPs with unbound carboxymaltose in solution. The observed up-turn in the 1:10 and 1:50 dilution data of IS and the observed down-turn in the stock solution of FCM is indicated with black arrows.

made up of single NPs and ii) unbound sucrose in solution (see Table 2 and SI for more details). The model describes the clusters as polydisperse prolate spheroids with an equatorial diameter of 2.0 nm and a polar diameter of 8.0 nm following a Gamma size distribution in both axes, made up of multiple single NPs of 2.0 nm.

The observed up-turn at low q in the 1:10 and 1:50 dilution curves of IS suggests the presence of large domains (> 100 nm) outside our analytical window. These domains were hypothesised to be related to the formation of agglomerates through the attachment of individual IS clusters, a phenomenon already partly observed in our cryo-STEM data (Fig. 1a, red arrows). The formation of larger structures was also seen in size-exclusion chromatography (SEC) measurements of IS upon dilution in phosphate buffer. In these, a shift of the typical IS peak (31 min, 34,000 Da) towards lower elution times (26 min, 192,000 Da) and a 6-fold increase in molecular weight was observed when an 1:2 dilution of IS was further diluted to 1:20, indicating the formation of higher-molecular-weight structures (Fig. S14, Table S3). Interestingly, no up-turn at low q was evident at an 1:100 dilution, likely due to agglomerates becoming too large to be observed in our analytical window. An explanation for the observed agglomerates can be the removal of the stabilising carbohydrate ligand during water dilution, impacting the colloidal stability of the IS clusters to promote their agglomeration. However, modelling of these domains is outside the scope of this study and would require additional ultra-small-angle scattering experiments for an extended q-range (< 0.01 nm^{-1}).

The size of the clusters was in agreement with previous dynamic light scattering (DLS) data of IS giving a hydrodynamic diameter of d_h = 8.3 nm [53]. However, polydispersity of clusters was significantly higher compared to the DLS data [49] of 1:50 diluted IS (48.2 vs 19.2%).

Table 2
Determined structural parameters from fitting small-angle x-ray scattering (SAXS) data of IS and FCM for different dilutions. Input parameters determined from cryo-STEM and x-ray diffraction (XRD) are given without confidence intervals. d_e [nm]: equatorial diameter of the spheroid, d_p [nm]: polar diameter of the spheroid, $PDI_{dp/de}$ [%]: polydispersity index of the polar and equatorial diameter, k: shape parameter of the Gamma size distribution, r: cluster radius [nm], Φ: volume fraction of the clusters, λ: screening length [nm], K: potential strength [J].

		Large cluster			Small cluster			Single NPs		
FCM	χ2	d_e	d_p	$PDI_{dp/de}$	d_e	d_p	$PDI_{dp/de}$	d_e	d_p	PDI_{dp}
stock	6.2	5.7	17. 0	38.1 ± 0.3	2.62 ± 0.02	5.2	21.0 ± 1.0	1.5	2.0	10.0
1:2	3.5	5.7	17.0	38.2 ± 0.3	2.62 ± 0.02	5.2	20.8 ± 0.6	1.5	2.0	10.0
1:10	27.1	5.7	17.0	34.0 ± 0.1	2.58 ± 0.02	5.2	19.0 ± 2.0	1.5	2.0	10.0
1:100	1.1	5.7	17.0	34.2 ± 0.1	3.24 ± 0.03	5.2	5.8 ± 2.7	1.5	2.0	10.0

Cluster interaction					
FCM	**r**	**Φ**	**λ**	**K**	**R**
stock	7.9	0.0122	0.25 ± 0.01	−29.9 ± 0.5	82.0
1:2	7.9	0.0062	0.18 ± 0.01	−30.7 ± 0.5	161.0

Cluster					
IS	**χ2**	**d_e**	**d_p**	**k**	**$PDI_{dp/de}$**
stock	2.2	2.0	8.0 ± 0.1	6.33 ± 0.02	47.2 ± 3.6
1:2	1.3	2.0	8.3 ± 0.1	6.25 ± 0.02	47.6 ± 3.6
1:10	1.1	2.0	9.1 ± 0.1	6.31 ± 0.02	47.3 ± 3.6
1:50	3.8	2.0	8.9 ± 0.2	6.15 ± 0.03	48.2 ± 3.6
1:100	2.1	2.0	9.9 ± 0.1	6.47 ± 0.03	46.5 ± 3.3

3.1.3.2. Ferric carboxymaltose. The SAXS curves of FCM (Fig. 3b) represented multi-component power law profiles typical for clustered and/or polydisperse systems at all dilution ratios, which is consistent with the broad size distributions observed in cryo-STEM. An inflection point at $q = 1\ nm^{-1}$ was observed, likely indicating the overlap between 2 or more scattering contributions from different populations of clusters as seen in cryo-STEM. For the less diluted curves (stock and 1:2), a down-turn was visible between $q = 0.03$ and $0.2\ nm^{-1}$, likely related to interactions between clusters.

To fit the scattering curves of FCM with an appropriate model, several assumptions based on the cryo-STEM and XRD data were used. The best obtained fit for FCM was realised with a hierarchical system of 4 components: i) large clusters made up of single NPs, ii) small clusters made up of single NPs, iii) free single NPs and iv) unbound carboxymaltose in solution (see Table 2 and SI). The model describes the large clusters as polydisperse prolate spheroids with an equatorial diameter of 5.7 nm and a polar diameter of 17.0 nm and the small clusters as polydisperse prolate spheroids with an equatorial diameter of 2.6 nm and a polar diameter of 5.2 nm with both following a Lognormal size distribution in both axes. The single NPs acting as building blocks for both types of clusters and the one's freely floating in solution, are described as polydisperse prolate spheroids with an equatorial diameter of 1.5 nm and a polar diameter of 2.0 nm following a Lognormal size distribution only in the long axis.

The model describes the observed down-turn at low q for a stock solution of FCM as interactions between large clusters through their arrangement at an average distance of 82.0 nm governed by electrostatic repulsion (Eq. S7). As indicated by the calculation of an experimental structure factor (Fig. S8a), this distance increases with increasing dilution from 82.0 to 161.3 nm, which is related to the increasing separation of large clusters. Higher-order peaks were non-existent, implying that large clusters arrange randomly and/or are highly polydisperse. The

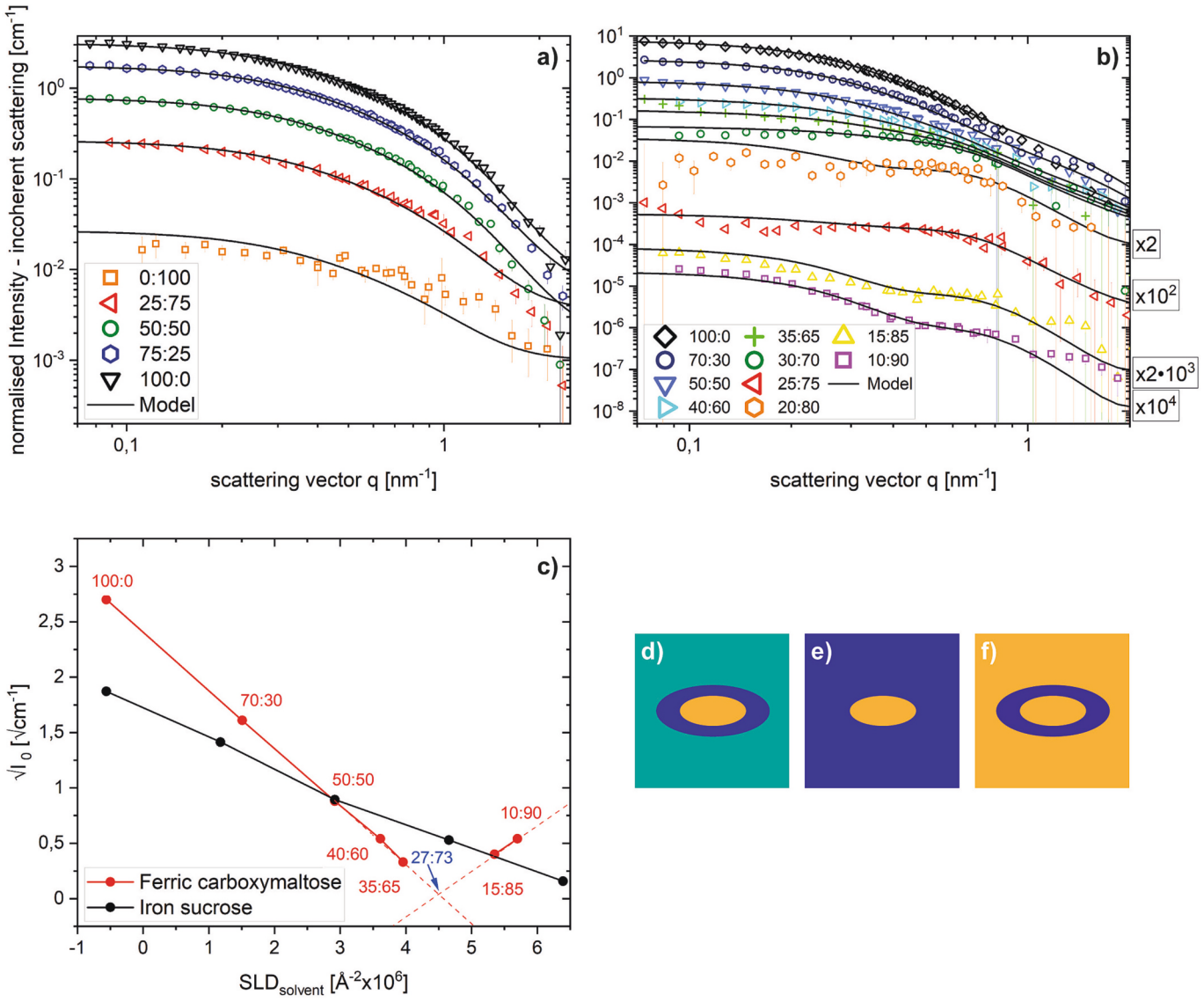

Fig. 4. Small-angle neutron scattering (SANS) data of iron-carbohydrate complexes with the corresponding model fits and analysis of the match point. (a) SANS data and model fits of IS for different ratios of H_2O to D_2O. The SANS model describes the carbohydrate ligand of IS as a diffuse and dynamic layer surrounding the prolate clusters of IS. (b) SANS data and model fits for an 1:10 dilution of FCM for different ratios of H_2O to D_2O. The SANS model describes the carbohydrate ligand of FCM as a localised ellipsoidal shell of 3.3 nm surrounding the large prolate clusters of FCM. (c) Analysis of the match point for IS (black) and for FCM (red). The local minimum is shown with a blue arrow. (d-f) Schematic representation of a contrast variation experiment of an ellipsoidal shell structure for three different H_2O to D_2O ratios. Different colours indicate different scattering length densities (SLDs) of the solvent. (d) refers to an H_2O to D_2O ratio of 90:10, (e) to a ratio of 54:46 and (f) to a ratio of 0.8:99.2 as indicated in (c) with red labels. Calculations for these ratios are found in the SI. (For interpretation of the references to colour in this figure legend, the reader is referred to the web version of this article.)

gradual decrease in inter-cluster interactions indicated by a gradual decrease in the observed down-turn was further evident when experimental SAXS curves for very low dilutions of FCM (97.5:25, 95:5 and 90:10) were measured (Fig. S8c and d). Interestingly, when FCM was measured at a very low q-range (< 0.04 nm^{-1}), a similar up-turn as already observed for IS, was evident (Fig. S8b). This was hypothesised to be related to FCM agglomerates in analogy to the observed IS agglomerates, which we did not incorporate in our model.

The large clusters' size was in agreement with previous DLS studies giving a hydrodynamic diameter of $d_h = 21.3$ nm [49]. However, polydispersity of large clusters was significantly higher compared to the DLS data of 1:125 diluted FCM (34.2 vs 7.0%).

Comparing our final models for IS and FCM, it was found that IS clusters were significantly smaller than FCM clusters, but had a higher aspect ratio. While the trend for the cluster size is in line with our cryo-STEM experiments, the trend for the aspect ratio differs. Here, cryo-STEM suggests IS to be less ellipsoidal and have a lower aspect ratio. A possible reason for this discrepancy in shape information between cryo-STEM and SAXS may be related to SAXS obtaining 3D information, while the STEM data are acquired as two-dimensional projections. The trend of the aspect ratios of the two complexes, determined from the SAXS models, was additionally supported by analysing the SAXS data in real space via the generalised indirect Fourier transform (GIFT) method (see SI, Fig. S9). The determined polydispersities of both IS and FCM clusters were generally higher than the values for existing DLS data but agreed with an increased polydispersity of IS compared to FCM [49,53].

When our model is compared to other SAXS studies on iron oxide NPs, hierarchical models are often applied. For instance, in a study on oleic acid-coated iron oxide NPs, a model was chosen that assumes spherical clusters built by spherical single NPs interacting through a structure factor with each other [54]. Other studies use a pearl-necklace model [55] or shape-independent models that assume fractal clusters [56]. These types of models were not used as the aim was to explain the shape of our system rather than their fractal structure.

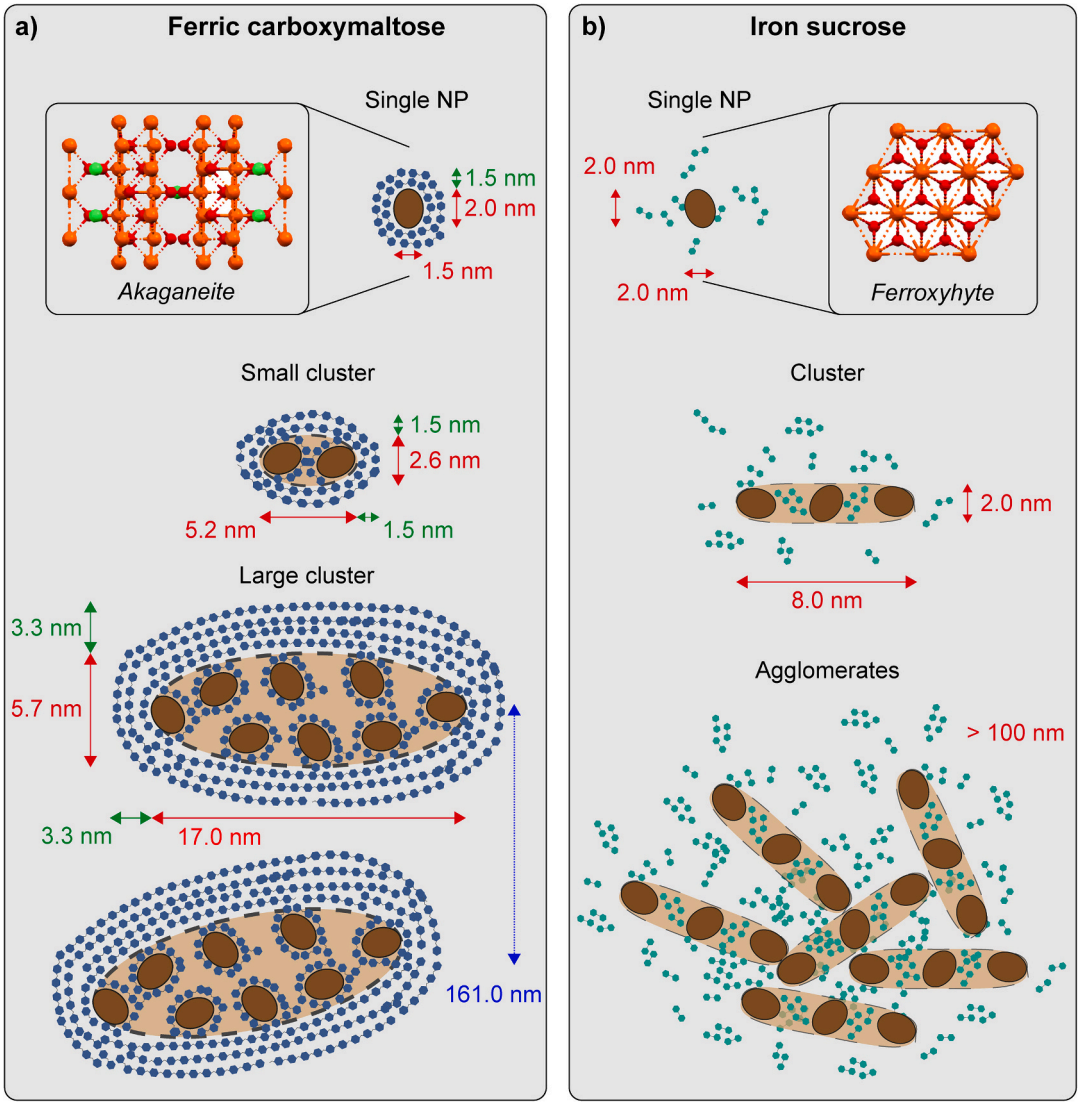

Fig. 5. Conclusive visualisation of the structural model based on the input data from cryo-STEM and XRD and further orthogonal analysis with SAXS and SANS for (a) FCM and (b) IS. The indicated numbers are average values calculated from the structural model and have a certain variance based on their respective polydispersity. Dark brown represents a single NP and light brown a cluster, while blue represents the carbohydrate ligand of FCM (i.e. carboxymaltose) and green the carbohydrate ligand of IS (i.e. sucrose). IS agglomerates are visualised based on the observed up-turn at low q-values for higher dilutions without application of a model. The blue arrow corresponds to the inter-cluster distance between large clusters of FCM. The carbohydrate shell is visualised for an 1:10 dilution of FCM. 3D models of crystal structures of IS and FCM single NPs are displayed in black windows. The size of carbohydrate structures was estimated by the known molecular size of a sucrose unit (9 Å) [58] and assumed to be intercalated in between single NPs within a cluster. Carbohydrate structures were created with *Biorender.com*. (For interpretation of the references to colour in this figure legend, the reader is referred to the web version of this article.)

3.1.4. Model of the nano-structure of the carbohydrate ligand

The goal of the SANS experiments was to resolve the shape, size and arrangement of the carbohydrate ligand surrounding the iron-carbohydrate complexes, which was not visible in SAXS due to a significantly lower SLD difference between the carbohydrate and the solvent compared to iron oxyhydroxide. Different dilution procedures were chosen for FCM and IS, respectively (see SI, Fig. S16).

3.1.4.1. Iron sucrose. For contrast variation of IS, the H_2O to D_2O ratio was varied from 0:100 to 100:0. With increasing D_2O ratio the scattering intensity gradually decreased due to changes in the SLD of the solvent. No indication of additional features such as oscillations from a monodisperse ellipsoidal or spherical shell structure was visible in any of the curves (Fig. 4a). For a theoretical polydisperse and heterogenous two-phase system (iron core and carbohydrate ligand), a local minimum is expected when analysing the match point (see SI). Such a local minimum was not observed for IS, indicating the absence of a scattering signal from bound carbohydrate ligand (Fig. 4c, black). Based on these findings, the best obtained fit for IS for all SANS curves was realised by using the same model as in the prior SAXS analysis. This model describes the carbohydrate ligand as a dynamic and diffuse layer surrounding the prolate and polydisperse clusters of IS. Thus, no significant scattering contribution of a localised carbohydrate shell is present around IS clusters (Fig. 5b).

3.1.4.2. Ferric carboxymaltose. For FCM, the H_2O to D_2O ratio was varied from 100:0 to 10:90 showing a gradual intensity decrease with increasing D_2O ratio until 25:75, from where it started to increase again. From this inflection point and for higher D_2O ratios, oscillations started to appear indicating the onset of an additional form factor (Fig. 4b). Analysis of the match point indicated a local minimum, estimated at an H_2O to D_2O ratio of 27:73, before the forward scattering increased again (Fig. 4c, red). This behaviour is typical for a polydisperse and heterogenous two-phase system and indicates the existence of bound carbohydrate ligand.

The best obtained fit for FCM for all SANS curves was therefore

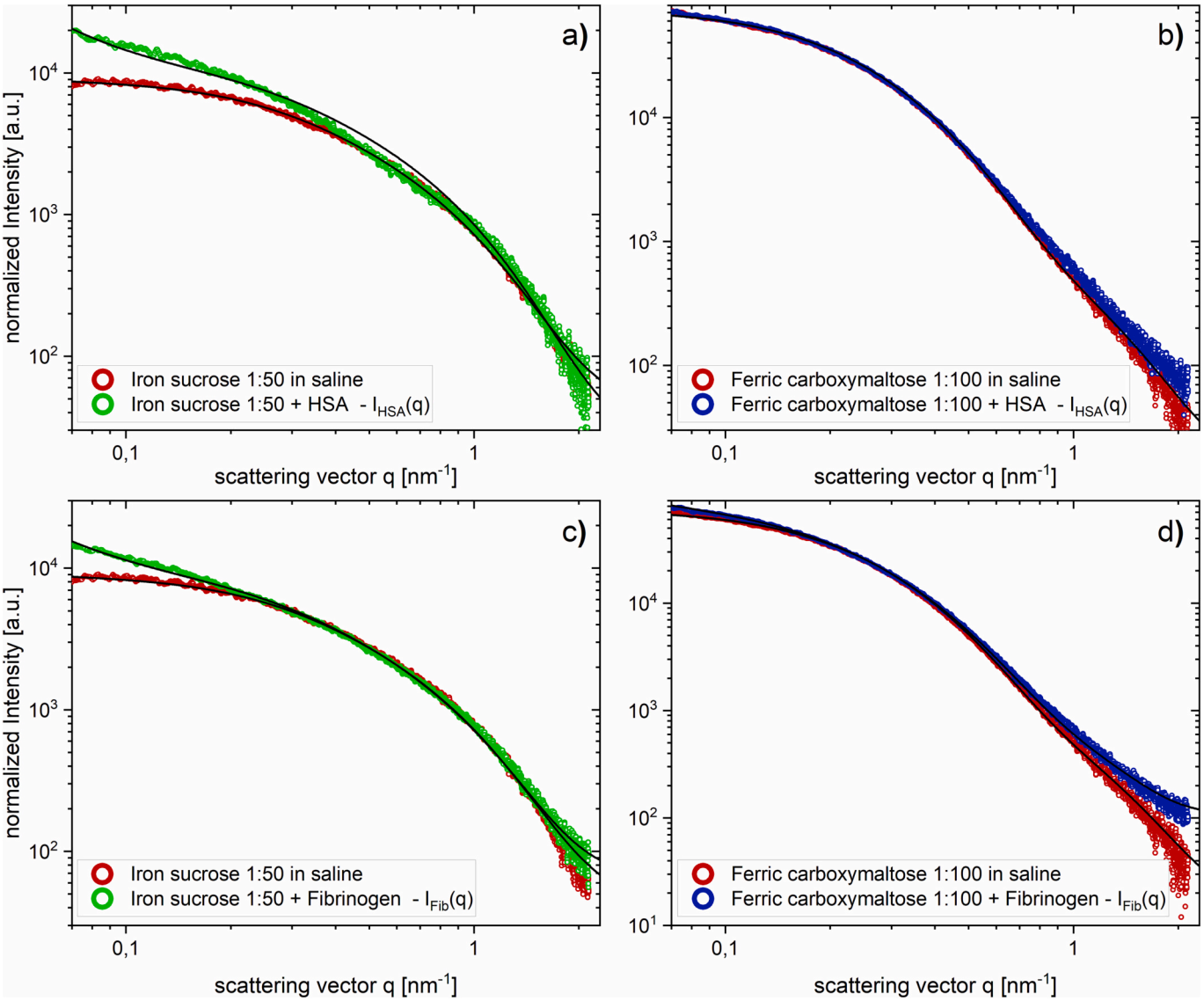

Fig. 6. SAXS data and model fits of human serum albumin (HSA) mixed with (a) IS (1:50) and (b) FCM (1:100) and fibrinogen mixed with (c) IS (1:50) and (d) FCM (1:100) in saline buffer. SAXS data of FCM (1:100) and IS (1:50) in saline buffer were added for comparison. The SAXS model indicates interaction of IS with both HSA and fibrinogen through formation of fractals from IS clusters and protein molecules. The same behaviour is observed for FCM but only with fibrinogen. Scattering contributions of pure HSA and fibrinogen were subtracted from the final data. SAXS data of the protein-NP mixtures were manually offset towards the background level of the pure NP solutions for better clarity.

realised by using the same model as in the prior SAXS analysis with an additional carbohydrate shell contribution (see SI). This model describes the carbohydrate ligand around the large clusters of FCM as a localised ellipsoidal shell with a constant thickness of 3.3 nm and a solvent content of 67% (Table S5). The carbohydrate ligand around both the small clusters and the single NPs of FCM is described by a localised ellipsoidal shell with a constant thickness of 1.5 nm and a solvent content of 67% (Fig. 5a). Interestingly, SANS curves for ratios of 30:70, 25:75 and 20:80 deviated from the model at $q < 0.3$ nm^{-1}, which may be related to interactions between the carbohydrate shell of large clusters, small clusters and single NPs. We refrained from modelling this with an additional structure factor as this would be outside the scope of our study.

The obtained overall equivalent diameter of 18.0 nm (Eq. S14) aligns with sizes from previous DLS analysis results ($d_h = 23.1$ nm, core + shell complex) [49]. Furthermore, the determined shell thickness for single NPs ($t = 1.5$ nm) matches the inter-particle distance observed in cryo-STEM (2.5–3.0 nm) when a 3.0 nm separation between neighbouring NPs with intercalating carbohydrate ligand is assumed. Our results also match well with existing atomic-force microscopy (AFM) data of IS and experimental AFM data of FCM as highly diluted IS showed an average diameter of 6.0 ± 2.0 nm [11], while three different batches of FCM showed a substantially higher average diameter of 20.9 ± 4.6 nm (Fig. S15 and Table S4).

Regarding the differences in surface morphologies between the two iron-carbohydrate complexes, the findings are in agreement with previous studies by NMR that look at the molecular interactions between the iron core and carbohydrate ligand [16,57]. While in IS the iron core mainly interacts through hydrogen bonding and van der Waals forces with its carbohydrate ligand, in FCM additional coordination bonds in the carbohydrate ligand are present, facilitating an increased interaction with the iron core through chelation [11,16,57]. This increases the overall number of interactions and makes the carbohydrate ligand of FCM more localised to its iron core compared to IS, which can be seen as a diffuse and dynamic layer of carbohydrate ligand.

3.2. *Interactions of iron-carbohydrate complexes with biological buffer and plasma proteins*

To look at the effect of biotransformation on the NP's structure, a solution of NaCl 0.9% *w/v* in milliQ-water was chosen as a buffer system since it is used for dilution of iron formulations during IV administration to the patient. The SAXS curves for 1:50 and 1:100 dilutions of IS and FCM in 0.9% *w/v* NaCl, respectively, as well as water are shown in Fig. S12. No clear difference was observed between the SAXS curves in milliQ-water and in 0.9% *w/v* NaCl for both iron-carbohydrate complexes, confirming the complex's colloidal stability in this buffer.

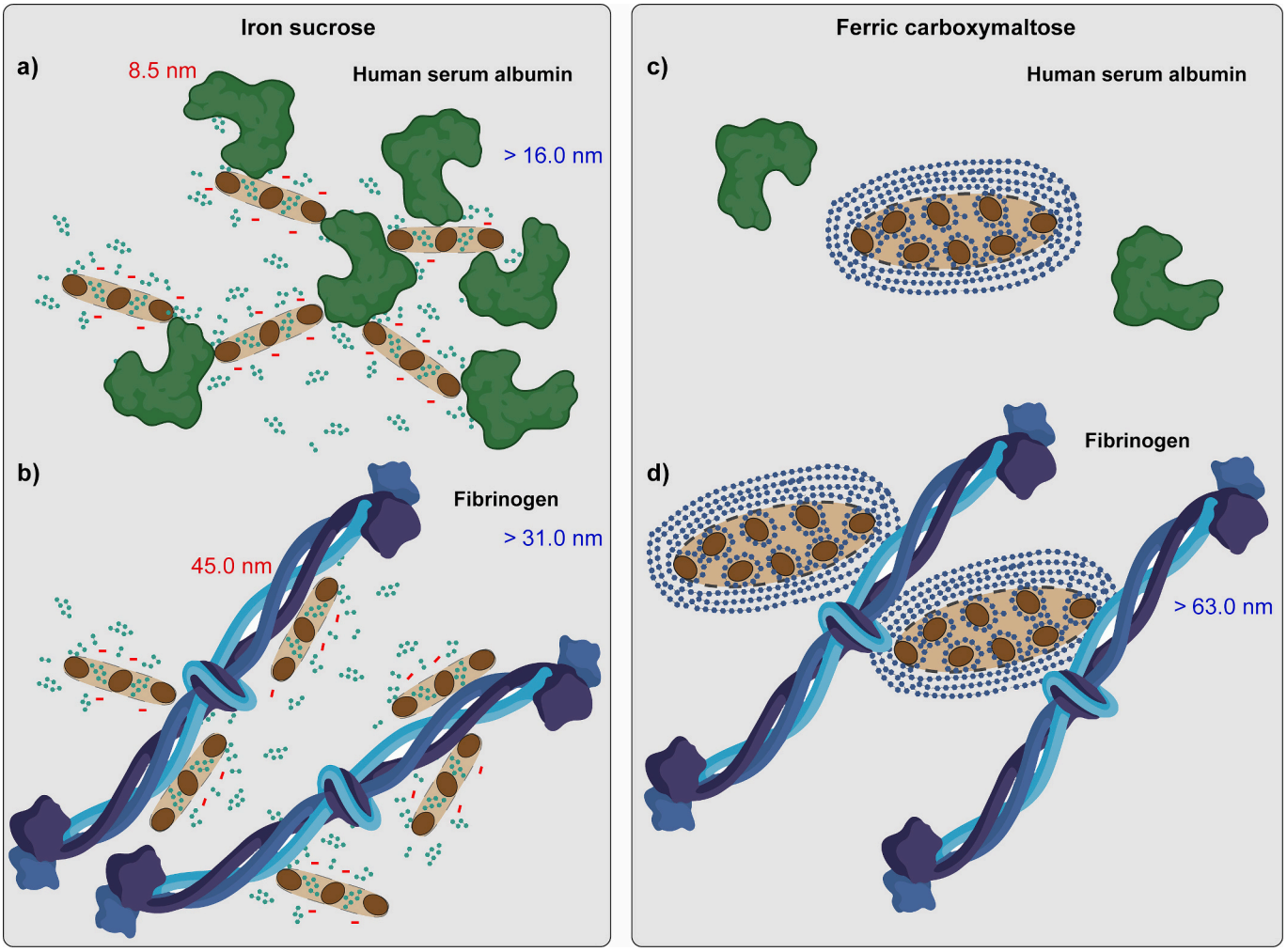

Fig. 7. Conclusive visualisation of the structural model describing the interaction of IS with (a) HSA and (b) fibrinogen and the interaction of FCM with (c) HSA and (d) fibrinogen through formation of fractal NP-protein clusters based on SAXS and SANS. Dark green represents an HSA protein molecule, while dark blue represents a fibrinogen glycoprotein. Red symbols or annotations indicate the size of the proteins and the surface charges of the iron-carbohydrate complexes known from Zeta potential studies [49]. Blue annotations indicate the estimated size of the NP-protein clusters. Protein structures were created with *Biorender.com*. (For interpretation of the references to colour in this figure legend, the reader is referred to the web version of this article.)

3.2.1. Human serum albumin (HSA) interaction

The interaction of both IS and FCM with HSA was studied at a nearly physiological HSA concentration with concentrations of IS and FCM resembling IV administration doses. Upon addition of the protein, an up-turn at low q was evident for a mixture of HSA and IS in saline (Fig. 6a) after subtracting the scattering contribution of pure HSA (Fig. S13a, green). The up-turn was described by the interaction of HSA molecules with IS clusters through random arrangement into fractal NP-protein clusters with estimated sizes >16.0 nm (fractal dimension = 2.2, scaling factor = $2.5 \bullet 10^{-3}$, Table S2, Eq. S10) and fitted using a simple power law (Eq. S11) as depicted in Fig. 6a. No evidence for a protein corona (cluster core and protein shell) as observed in other studies [59], was found in our observation window. Because no correlation peaks were observed in measurements at a very low q-range (0.03–0.2 nm^{-1}), ordered self-assembled structures from clusters and HSA, as seen in studies with gold NPs [60], were also ruled out (Fig. S13b). As proteins have the same size (HSA, 8.5 nm [61]) or a bigger size (fibrinogen, 45.0 nm [46]) compared to both iron-carbohydrate complex clusters, agglomeration caused by a depletion effect of the protein molecules was excluded. When looking at the interaction of FCM with HSA, no changes in the scattering curves were observed for a mixture of FCM and HSA in saline, indicating a lack of interaction (Fig. 6b).

3.2.2. Fibrinogen interaction

The interaction of both iron-carbohydrate complexes with the much bigger-sized and elongated macromolecule, fibrinogen, was investigated at a physiological protein concentration. Similarly, an up-turn for fibrinogen was observed after subtraction of the scattering of pure fibrinogen (Fig. S13a, blue), but this time for both complexes. The up-turn was described by the interaction of fibrinogen molecules with iron-carbohydrate complex clusters through random arrangement into fractal NP-protein clusters and fitted with the same model as for HSA (Eq. S11) as depicted in Fig. 6c and d. It was found that IS clusters undergo a stronger interaction with fibrinogen compared to the clusters of FCM. This is indicated by a 5-fold increase in the up-turn for IS compared to FCM (a = $4.0 \bullet 10^{-3}$ vs. $8.0 \bullet 10^{-4}$, Table S2), while the arrangement of the NP-protein clusters was the same for both complexes (fractal dimension = 2.0).

The significant difference in HSA interaction between IS and FCM can be related to the difference in the surface morphology of their respective carbohydrate ligand (Fig. 7a and c). Since IS has a dynamic and diffuse layer of carbohydrate ligand, as observed in our SANS measurements, proteins can easily absorb or interact with the iron core of IS as no electrostatic or steric forces are present. In contrast, the localised carbohydrate shell of FCM causes a sterical or electrostatic barrier hindering the interaction with HSA. The difference in HSA interaction is also explained by differences in the surface charge and functionalisation of IS and FCM. IS has a negative Zeta potential at pH values between 4 and 11 together with a high amount of deprotonated hydroxy groups [16,49]. This facilitates interaction with site I (warfarin site) on domain II of HSA, known to interact with negatively charged compounds [62]. This is not the case for FCM, where a Zeta potential close to zero is observed at pH values lower than 7 and most of the hydroxy groups are protonated.

The difference in fibrinogen interaction between FCM and IS was explained by differing surface morphologies of the iron-carbohydrate complexes as discussed before (Fig. 7b and d). Surface charge differences of the iron-carbohydrates complexes should not play a role here, as fibrinogen possesses domains interacting both with negatively charged (D and E domain) and positively charged compounds (aC-chain) [63]. However, this does not explain the difference in interaction when FCM is mixed with HSA compared to fibrinogen, which should be related to the difference in shape, size or the binding affinity of the proteins. For instance, Canoa et al. observed significantly higher binding affinities between fibrinogen and Al_2O_3, TiO_2 and CeO_2 NPs compared to HSA via surface plasmon resonance [64], agreeing with our results.

4. Conclusion

In this study, we further explored and modelled the nano-structure and individual building blocks of two clinically relevant iron-carbohydrate complexes, IS and FCM. Although iron-carbohydrate complexes have been on the market for over seven decades, only now a more comprehensive structural understanding of the iron core and the surrounding carbohydrate ligand of the two formulations becomes available. We found differences in the nano-structure between both iron-carbohydrate complexes apparent in their cluster formation, crystallinity and carbohydrate ligand morphology. Additionally, we observed differences in serum protein interactions between the two formulations and hypothesise the difference in carbohydrate ligand morphology plays a key role in their protein interaction behaviours. This discrepancy in serum protein interactions may, in turn, affect how the two formulations are perceived in the bloodstream, with FCM potentially being recognized as a bare cluster with a carbohydrate surface, while IS as a NP-protein cluster. This could explain differences in bio-responses, such as changes in clearance kinetics from serum, macrophage uptake and release rates of bioactive iron from the NP [27,39].

For the methodology employed in this study, it was essential to combine morphological information from cryo-STEM with high-statistics data from SAXS to characterise the iron core and complement these data with SANS to elucidate the carbohydrate ligand morphology.

The methods described in this study have the potential to further refine the critical quality attributes (CQAs) for the complex class of iron-carbohydrate nanomedicines, in particular ligand morphology, which remains poorly described. They are also applicable to other NBCDs and clinically relevant core-shell systems with organic surface structures. This orthogonal approach can facilitate a more detailed understanding of the impact of small variations in physicochemical characteristics (i.e. CQAs) on relevant biological interactions in vivo and ultimately clinical outcomes. It provides the scientific foundation to further explore the dynamic behaviour of iron-carbohydrate complexes in more complex bio-relevant systems such as protein-rich whole blood or the highly acidic environment within cell lysosomes.

Author contributions

The manuscript was written through contributions of all authors. All authors have given approval to the final version of the manuscript. Conceptualisation: LK, AN, ML and PW. LK coordinated and initiated the orthogonal approach of the study (cryo-STEM, SAXS, SANS, SEC, AFM and XRD); Methodology: LK; Investigation: LK carried out the SAXS experiments. ML, JA, CA, CB and NA collected the synchrotron SAXS data. LK, NA, ML and JK collected the SANS data. AS and SH carried out the cryo-STEM experiments. EP provided the SEC and AFM data; Formal analysis: LK analysed the SAXS and SANS data. LK and AN analysed the XRD data. LK, AR and AS analysed the cryo-STEM data. TT carried out the statistical analysis of the cryo-STEM data; Validation: LK; Software: LK, JA, AR and TT; Resources: AN and PW; Data Curation: LK; Writing – Original Draft: LK; Visualisation: LK prepared all figures and visualisations. AS prepared Fig. S1 and S2; Supervision: AN, ML and PW; Writing – Review & Editing: LK, JA, ML, AN, PW, AA, CA, RD, BS, AS and TT; Project administration: PW, ML, AN and BF; Funding acquisition: PW, BF and EP.

Funding

This study was funded by CSL Vifor, Switzerland. BF, AA, EP and RD are employees of CSL Vifor. CA acknowledges the funding received from the European Union's Horizon 2020 research and innovation program under the Marie Sklodowska-Curie grant agreement No 884104 and Chalmers initiative for advancement of neutron and X-ray techniques.

Data availability

The data supporting the findings of this study are not openly available due to reasons of sensitivity and are available from the corresponding author upon reasonable request. The data are located in the controlled access data storage of Empa, St. Gallen.

The following files are available free of charge.

Supporting Information (SI):

- SAXS and SANS experimental details, methodology, data analysis, model details and assumptions, fitting procedure and additional SAXS and SANS data
- cryo-STEM methodology, EDS methodology, experimental details, automated and manual analysis, statistical analysis and additional cryo-STEM data
- XRD data analysis
- size-exclusion chromatography methodology and data
- AFM methodology and data

Acknowledgements

The authors acknowledge the Paul Scherrer Institute, Villigen PSI, Switzerland for provision of synchrotron radiation beam-time at the beamline cSAXS of the SLS. This work is based on experiments performed at the Swiss spallation neutron source SINQ, Paul Scherrer Institute, Villigen, Switzerland. We acknowledge DESY (Hamburg, Germany), a member of the Helmholtz Association HGF, for the provision of experimental facilities. Parts of this research were carried out at PETRA III and we would like to thank CB for assistance in using the P12 beamline of EMBL. We acknowledge Patrick Rupper and Liliane Diener for performing the AFM experiments and providing us with the corresponding data analysis. We also acknowledge Alex Dommann for discussions on the investigation of the study.

Appendix A. Supplementary data

Supplementary data to this article can be found online at https://doi.org/10.1016/j.jconrel.2024.02.044.

References

[1] De Benoist, B.; Cogswell, M.; Egli, I.; McLean, E. Worldwide Prevalence of Anaemia 1993-2005; WHO Global Database of Anaemia. 2008.
[2] M. Muñoz, S. Gómez-Ramírez, G.M. Liumbruno, G. Grazzini, Intravenous iron and safety: is the end of the debate on the horizon? Blood Transfus. 12 (3) (2014) 287–289, https://doi.org/10.2450/2014.0144-14.
[3] I.C. Macdougall, J. Comin-Colet, C. Breymann, D.R. Spahn, I.E. Koutroubakis, Iron sucrose: a wealth of experience in treating iron deficiency, Adv. Ther. 37 (5) (2020) 1960–2002, https://doi.org/10.1007/s12325-020-01323-z.
[4] M.D. Cappellini, K.M. Musallam, A.T. Taher, Iron deficiency anaemia revisited, J. Intern. Med. 287 (2) (2020) 153–170, https://doi.org/10.1111/joim.13004.
[5] V. Weissig, T.K. Pettinger, N. Murdock, Nanopharmaceuticals (part 1): products on the market, Int. J. Nanomedicine 9 (2014) 4357–4373, https://doi.org/10.2147/IJN.S46900.
[6] N. Nikravesh, G. Borchard, H. Hofmann, E. Philipp, B. Flühmann, P. Wick, Factors influencing safety and efficacy of intravenous iron-carbohydrate nanomedicines: from production to clinical practice, Nanomed. Nanotechnol. Biol. Med. 26 (2020) 102178, https://doi.org/10.1016/j.nano.2020.102178.
[7] A. Grzywacz, A. Lubas, P. Fiedor, M. Fiedor, S. Niemczyk, Safety and efficacy of intravenous administration of iron preparations, Acta Pol. Pharm. 74 (2017) 13–24.
[8] M. Auerbach, H. Ballard, Clinical use of intravenous iron: administration, efficacy, and safety, Hematology 2010 (1) (2010) 338–347, https://doi.org/10.1182/asheducation-2010.1.338.
[9] J. Eduardo Toblli, G. Cao, L. Oliveri, M. Angerosa, Comparison of oxidative stress and inflammation induced by different intravenous Iron sucrose similar preparations in a rat model, Inflamm. Allergy – Drug Targets Former. Curr. Drug Targets – Inflamm. Allergy 11 (1) (2012) 66–78, https://doi.org/10.2174/187152812798889358.
[10] J. García-Fernández, J. Bettmer, N. Jakubowski, U. Panne, E. Añón, M. Montes-Bayón, A. Sanz-Medel, The fate of Iron nanoparticles used for treatment of iron deficiency in blood using mass-spectrometry based strategies, Microchim. Acta 184 (10) (2017) 3673–3680, https://doi.org/10.1007/s00604-017-2388-8.
[11] D.S. Kudasheva, J. Lai, A. Ulman, M.K. Cowman, Structure of carbohydrate-bound polynuclear iron oxyhydroxide nanoparticles in parenteral formulations, J. Inorg. Biochem. 98 (11) (2004) 1757–1769, https://doi.org/10.1016/j.jinorgbio.2004.06.010.
[12] A.D. McNaught, A. Wilkinson, Compendium of Chemical Terminology 1669, Blackwell Science Oxford, 1997.
[13] S. Mühlebach, B. Flühmann, Iron carbohydrate complexes: characteristics and regulatory challenges, in: D.J.A. Crommelin, J.S.B. de Vlieger (Eds.), Non-Biological Complex Drugs: The Science and the Regulatory Landscape, Springer International Publishing, Cham, 2015, pp. 149–170, https://doi.org/10.1007/978-3-319-16241-6_5. AAPS Advances in the Pharmaceutical Sciences Series.
[14] G. Borchard, B. Flühmann, S. Mühlebach, Nanoparticle Iron medicinal products – requirements for approval of intended copies of non-biological complex drugs (NBCD) and the importance of clinical comparative studies, Regul. Toxicol. Pharmacol. 64 (2) (2012) 324–328, https://doi.org/10.1016/j.yrtph.2012.08.009.
[15] F. Funk, K. Weber, N. Nyffenegger, J.-A. Fuchs, A. Barton, Tissue biodistribution of intravenous iron-carbohydrate nanomedicines differs between preparations with varying physicochemical characteristics in an anemic rat model, Eur. J. Pharm. Biopharm. 174 (2022) 56–76, https://doi.org/10.1016/j.ejpb.2022.03.006.
[16] F. Funk, B. Flühmann, A.E. Barton, Criticality of surface characteristics of intravenous iron–carbohydrate nanoparticle complexes: implications for pharmacokinetics and pharmacodynamics, Int. J. Mol. Sci. 23 (4) (2022) 2140, https://doi.org/10.3390/ijms23042140.
[17] A.T. Goetsch, C.V. Moore, V. Minnich, Observations on the effect of massive doses of iron given intravenously to patients with hypochromic anemia, Blood 1 (2) (1946) 129–142.
[18] P. Geisser, S. Burckhardt, The pharmacokinetics and pharmacodynamics of iron preparations, Pharmaceutics 3 (1) (2011) 12–33, https://doi.org/10.3390/pharmaceutics3010012.
[19] F. Funk, P. Ryle, C. Canclini, S. Neiser, P. Geisser, The new generation of intravenous iron: chemistry, pharmacology, and toxicology of ferric carboxymaltose, Arzneimittelforschung 60 (6) (2010) 345–353, https://doi.org/10.1055/s-0031-1296299.
[20] B.G. Danielson, Structure, chemistry, and pharmacokinetics of intravenous iron agents, J. Am. Soc. Nephrol. 15 (Suppl. 2) (2004) S93–S98, https://doi.org/10.1097/01.ASN.0000143814.49713.C5.
[21] E. Alphandéry, Iron oxide nanoparticles for therapeutic applications, Drug Discov. Today 25 (1) (2020) 141–149, https://doi.org/10.1016/j.drudis.2019.09.020.
[22] D. Sun, R. Rouse, V. Patel, Y. Wu, J. Zheng, A. Karmakar, A.K. Patri, P. Chitranshi, D. Keire, J. Ma, W. Jiang, Comparative evaluation of U.S. brand and generic intravenous sodium ferric gluconate complex in sucrose injection: physicochemical characterization, Nanomaterials 8 (1) (2018) 25, https://doi.org/10.3390/nano8010025.
[23] J. Rottembourg, A. Kadri, E. Leonard, A. Dansaert, A. Lafuma, Do two intravenous iron sucrose preparations have the same efficacy? Nephrol. Dial. Transplant. 26 (10) (2011) 3262–3267, https://doi.org/10.1093/ndt/gfr024.
[24] T.S. Koskenkorva-Frank, G. Weiss, W.H. Koppenol, S. Burckhardt, The complex interplay of iron metabolism, reactive oxygen species, and reactive nitrogen species: insights into the potential of various iron therapies to induce oxidative and nitrosative stress, Free Radic. Biol. Med. 65 (2013) 1174–1194, https://doi.org/10.1016/j.freeradbiomed.2013.09.001.
[25] J. Bossart, A. Rippl, A.E. Barton Alston, B. Flühmann, R. Digigow, M. Buljan, V. Ayala-Nunez, P. Wick, Uncovering the dynamics of cellular responses induced by iron-carbohydrate complexes in human macrophages using quantitative proteomics and phosphoproteomics, Biomed. Pharmacother. 166 (2023) 115404, https://doi.org/10.1016/j.biopha.2023.115404.
[26] F.M. Torti, S.V. Torti, Regulation of ferritin genes and protein, Blood 99 (10) (2002) 3505–3516, https://doi.org/10.1182/blood.V99.10.3505.
[27] A. Milosevic, D. Romeo, P. Wick, Understanding nanomaterial biotransformation: an unmet challenge to achieving predictive nanotoxicology, Small 16 (36) (2020) 1907650, https://doi.org/10.1002/smll.201907650.
[28] T.L. Moore, L. Rodriguez-Lorenzo, V. Hirsch, S. Balog, D. Urban, C. Jud, B. Rothen-Rutishauser, M. Lattuada, A. Petri-Fink, Nanoparticle colloidal stability in cell culture media and impact on cellular interactions, Chem. Soc. Rev. 44 (17) (2015) 6287–6305, https://doi.org/10.1039/C4CS00487F.
[29] T. Cedervall, I. Lynch, S. Lindman, T. Berggård, E. Thulin, H. Nilsson, K.A. Dawson, S. Linse, Understanding the nanoparticle–protein corona using methods to quantify exchange rates and affinities of proteins for nanoparticles, Proc. Natl. Acad. Sci. 104 (7) (2007) 2050–2055, https://doi.org/10.1073/pnas.0608582104.
[30] M. Lundqvist, J. Stigler, G. Elia, I. Lynch, T. Cedervall, K.A. Dawson, Nanoparticle size and surface properties determine the protein Corona with possible implications for biological impacts, Proc. Natl. Acad. Sci. 105 (38) (2008) 14265–14270, https://doi.org/10.1073/pnas.0805135105.
[31] C. Röcker, M. Pötzl, F. Zhang, W.J. Parak, G.U. Nienhaus, A quantitative fluorescence study of protein monolayer formation on colloidal nanoparticles, Nat. Nanotechnol. 4 (9) (2009) 577–580, https://doi.org/10.1038/nnano.2009.195.
[32] X. Jiang, S. Weise, M. Hafner, C. Röcker, F. Zhang, W.J. Parak, G.U. Nienhaus, Quantitative analysis of the protein Corona on FePt nanoparticles formed by transferrin binding, J. R. Soc. Interface 7 (suppl_1) (2010) S5–S13.
[33] C. Rehbock, V. Merk, L. Gamrad, R. Streubel, S. Barcikowski, Size control of laser-fabricated surfactant-free gold nanoparticles with highly diluted electrolytes and their subsequent bioconjugation, Phys. Chem. Chem. Phys. 15 (9) (2013) 3057–3067, https://doi.org/10.1039/C2CP42641B.
[34] S. Kittler, C. Greulich, J.S. Gebauer, J. Diendorf, L. Treuel, L. Ruiz, J.M. Gonzalez-Calbet, M. Vallet-Regi, R. Zellner, M. Köller, M. Epple, The influence of proteins on the dispersability and cell-biological activity of silver nanoparticles, J. Mater. Chem. 20 (3) (2009) 512–518, https://doi.org/10.1039/B914875B.

[35] J.S. Gebauer, M. Malissek, S. Simon, S.K. Knauer, M. Maskos, R.H. Stauber, W. Peukert, L. Treuel, Impact of the nanoparticle–protein Corona on colloidal stability and protein structure, Langmuir 28 (25) (2012) 9673–9679, https://doi.org/10.1021/la301104a.
[36] A. Albanese, C.D. Walkey, J.B. Olsen, H. Guo, A. Emili, W.C.W. Chan, Secreted biomolecules alter the biological identity and cellular interactions of nanoparticles, ACS Nano 8 (6) (2014) 5515–5526, https://doi.org/10.1021/nn4061012.
[37] D. Hühn, K. Kantner, C. Geidel, S. Brandholt, I. De Cock, S.J.H. Soenen, P. Rivera Gil, J.-M. Montenegro, K. Braeckmans, K. Müllen, G.U. Nienhaus, M. Klapper, W. J. Parak, Polymer-coated nanoparticles interacting with proteins and cells: focusing on the sign of the net charge, ACS Nano 7 (4) (2013) 3253–3263, https://doi.org/10.1021/nn3059295.
[38] D. Docter, D. Westmeier, M. Markiewicz, S. Stolte, S.K. Knauer, R.H. Stauber, The nanoparticle biomolecule Corona: lessons learned – challenge accepted? Chem. Soc. Rev. 44 (17) (2015) 6094–6121, https://doi.org/10.1039/C5CS00217F.
[39] B. Fadeel, A. Fornara, M.S. Toprak, K. Bhattacharya, Keeping it real: The importance of material characterization in nanotoxicology, Biochem. Biophys. Res. Commun. 468 (3) (2015) 498–503, https://doi.org/10.1016/j.bbrc.2015.06.178.
[40] Research, C. for D. E, Drug Products, Including Biological Products, that Contain Nanomaterials –Guidance for Industry. https://www.fda.gov/regulatory-information/search-fda-guidance-documents/drug-products-including-biological-products-contain-nanomaterials-guidance-industry.
[41] EMA. *Reflection Paper on the Data Requirements for Intravenous Iron-Based Nano-Colloidal Products Developed with Reference to an Innovator Medicinal Product.* http://www.ema.europa.eu/docs/en_GB/document_library/Scientific_guideline/2015/03/WC500184922.pdf (accessed 2024-02-10).
[42] L. Krupnik, P. Joshi, A. Kappler, B. Flühmann, A.B. Alston, R. Digigow, P. Wick, A. Neels, Critical nanomaterial attributes of iron-carbohydrate nanoparticles: leveraging orthogonal methods to resolve the 3-dimensional structure, Eur. J. Pharm. Sci. 188 (2023) 106521, https://doi.org/10.1016/j.ejps.2023.106521.
[43] C. Moya, R. Escudero, D.C. Malaspina, M. de la Mata, J. Hernández-Saz, J. Faraudo, A. Roig, Insights into preformed human serum albumin Corona on iron oxide nanoparticles: structure, effect of particle size, impact on MRI efficiency, and metabolization, ACS Appl. Bio Mater. 2 (7) (2019) 3084–3094, https://doi.org/10.1021/acsabm.9b00386.
[44] J. Mariam, S. Sivakami, P.M. Dongre, Albumin Corona on nanoparticles - a strategic approach in drug delivery, Drug Deliv. 23 (8) (2016) 2668–2676, https://doi.org/10.3109/10717544.2015.1048488.
[45] G. Fanali, A. di Masi, V. Trezza, M. Marino, M. Fasano, P. Ascenzi, Human serum albumin: from bench to bedside, Mol. Aspects Med. 33 (3) (2012) 209–290, https://doi.org/10.1016/j.mam.2011.12.002.
[46] M.W. Mosesson, Fibrinogen and fibrin structure and functions, J. Thromb. Haemost. 3 (8) (2005) 1894–1904, https://doi.org/10.1111/j.1538-7836.2005.01365.x.
[47] S. Herrick, O. Blanc-Brude, A. Gray, G. Laurent, Fibrinogen, Int. J. Biochem. Cell Biol. 31 (7) (1999) 741–746, https://doi.org/10.1016/S1357-2725(99)00032-1.
[48] U. Keiderling, The new 'BerSANS-PC' software for reduction and treatment of small angle neutron scattering data, Appl. Phys. A Mater. Sci. Process. 74 (1) (2002) s1455–s1457, https://doi.org/10.1007/s003390201561.
[49] M.R. Jahn, H.B. Andreasen, S. Fütterer, T. Nawroth, V. Schünemann, U. Kolb, W. Hofmeister, M. Muñoz, K. Bock, M. Meldal, P. Langguth, A comparative study of the physicochemical properties of iron isomaltoside 1000 (Monofer®), a new intravenous Iron preparation and its clinical implications, Eur. J. Pharm. Biopharm. 78 (3) (2011) 480–491, https://doi.org/10.1016/j.ejpb.2011.03.016.
[50] Y. Wu, P. Petrochenko, L. Chen, S.Y. Wong, M. Absar, S. Choi, J. Zheng, Core size determination and structural characterization of intravenous iron complexes by cryogenic transmission electron microscopy, Int. J. Pharm. 505 (1–2) (2016) 167–174, https://doi.org/10.1016/j.ijpharm.2016.03.029.
[51] S. Neiser, D. Rentsch, U. Dippon, A. Kappler, P.G. Weidler, J. Göttlicher, R. Steininger, M. Wilhelm, M. Braitsch, F. Funk, E. Philipp, S. Burckhardt, Physico-chemical properties of the new generation IV iron preparations ferumoxytol, iron isomaltoside 1000 and ferric carboxymaltose, BioMetals 28 (4) (2015) 615–635, https://doi.org/10.1007/s10534-015-9845-9.
[52] S. Fütterer, I. Andrusenko, U. Kolb, W. Hofmeister, P. Langguth, Structural characterization of iron oxide/hydroxide nanoparticles in nine different parenteral drugs for the treatment of iron deficiency anaemia by electron diffraction (ED) and X-ray powder diffraction (XRPD), J. Pharm. Biomed. Anal. 86 (2013) 151–160, https://doi.org/10.1016/j.jpba.2013.08.005.
[53] T.D. Francesco, E. Philipp, G. Borchard, Iron sucrose: assessing the similarity between the originator drug and its intended copies, Ann. N. Y. Acad. Sci. 1407 (1) (2017) 63–74, https://doi.org/10.1111/nyas.13517.
[54] C. Appel, B. Kuttich, L. Stühn, R.W. Stark, B. Stühn, Structural properties and magnetic ordering in 2D polymer nanocomposites: existence of long magnetic dipolar chains in zero field, Langmuir 35 (37) (2019) 12180–12191, https://doi.org/10.1021/acs.langmuir.9b02094.
[55] M. Bonini, E. Fratini, P. Baglioni, SAXS study of chain-like structures formed by magnetic nanoparticles, Mater. Sci. Eng. C 27 (5) (2007) 1377–1381, https://doi.org/10.1016/j.msec.2006.09.002.
[56] A.L. Rose, M.W. Bligh, R.N. Collins, T.D. Waite, Resolving early stages of homogeneous iron(III) oxyhydroxide formation from Iron(III) nitrate solutions at pH 3 using time-resolved SAXS, Langmuir 30 (12) (2014) 3548–3556, https://doi.org/10.1021/la404712r.
[57] X. Kästele, C. Sturm, P. Klüfers, 13C NMR spectroscopy as a tool for the in situ characterisation of Iron-supplementing preparations, Eur. J. Pharm. Biopharm. 86 (3) (2014) 469–477, https://doi.org/10.1016/j.ejpb.2013.11.003.
[58] C.A. Beevers, T.R.R. McDonald, J.H. Robertson, F. Stern, The crystal structure of sucrose, Acta Crystallogr. 5 (5) (1952) 689–690, https://doi.org/10.1107/S0365110X52001908.
[59] J. Wang, U.B. Jensen, G.V. Jensen, S. Shipovskov, V.S. Balakrishnan, D. Otzen, J. S. Pedersen, F. Besenbacher, D.S. Sutherland, Soft interactions at nanoparticles alter protein function and conformation in a size dependent manner, Nano Lett. 11 (11) (2011) 4985–4991, https://doi.org/10.1021/nl202940k.
[60] Iranpour Anaraki, N.; Liebi, M.; Ong, Q.; Blanchet, C.; Maurya, A. K.; Stellacci, F.; Salentinig, S.; Wick, P.; Neels, A. In-Situ investigations on gold nanoparticles stabilization mechanisms in biological environments containing HSA. *Adv. Funct. Mater. n/a* (n/a), 2110253. https://doi.org/10.1002/adfm.202110253.
[61] M.A. Kiselev, I.A. Gryzunov, G.E. Dobretsov, M.N. Komarova, Size of a human serum albumin molecule in solution, Biofizika 46 (3) (2001) 423–427.
[62] G. Colmenarejo, In silico prediction of drug-binding strengths to human serum albumin, Med. Res. Rev. 23 (3) (2003) 275–301, https://doi.org/10.1002/med.10039.
[63] C. Yongli, Z. Xiufang, G. Yandao, Z. Nanming, Z. Tingying, S. Xinqi, Conformational changes of fibrinogen adsorption onto hydroxyapatite and titanium oxide nanoparticles, J. Colloid Interface Sci. 214 (1) (1999) 38–45, https://doi.org/10.1006/jcis.1999.6159.
[64] P. Canoa, R. Simón-Vázquez, J. Popplewell, Á. González-Fernández, A quantitative binding study of fibrinogen and human serum albumin to metal oxide nanoparticles by surface plasmon resonance, Biosens. Bioelectron. 74 (2015) 376–383, https://doi.org/10.1016/j.bios.2015.05.070.